

Magnetic Structure and Properties of the Na₂CoP₂O₇ Pyrophosphate Cathode for Sodium-ion Batteries: a Super-superexchange Driven Non-Collinear Antiferromagnet

Prabeer Barpanda,^{a,†*} Maxim Avdeev,^{b,†} Chris D. Ling,^c
Jiechen Lu,^a Atsuo Yamada^{a,d}

a. Department of Chemical System Engineering, The University of Tokyo,
Building 5-604, 7-3-1 Hongo, Bunkyo-ku, Tokyo 113-8656, Japan.

b. Bragg Institute, B87, Australian Nuclear Science and Technology Organisation,
Locked Bag 2001, Kirrawee DC NSW 2232, Australia.

c. School of Chemistry, The University of Sydney, Sydney, NSW 2006, Australia.

d. Unit of Elements Strategy Initiative for Catalysts & Batteries, ESICB,
Kyoto University, Kyoto 615-8510, Japan.

† authors with equal contribution

* prabeer@chemsys.t.u-tokyo.ac.jp

Phone: +81-3-5841-7295; Fax: +81-3-5841-7488

Abstract

The crystal and magnetic structure and properties of the Na₂CoP₂O₇ sodium-ion battery cathode material have been characterized by magnetic susceptibility, specific heat, and variable temperature neutron powder diffraction measurements. Na₂CoP₂O₇ crystallizes in the orthorhombic space group *Pna*2₁ with *a* = 15.4061(3) Å, *b* = 10.28854(9) Å and *c* = 7.70316(15) Å, having a layered structure with slabs of [CoP₂O₇]_∞ separated by Na cations. The magnetic property measurements and neutron diffraction data analysis reveal that the material undergoes long-range ordering to a non-collinear antiferromagnetic G-type structure below T_N ~ 6.5 K. The magnetic structure is rationalized as a result of super-superexchange between Co²⁺ atoms linked by phosphate groups.

Keywords: pyrophosphates, Na₂CoP₂O₇, magnetic structure, neutron diffraction.

Introduction:

Combating the demand for mobile energy supply to empower portable consumer electronics and (plug-in hybrid) electric vehicles, various electrochemical energy storage devices have been widely explored, Li-ion batteries being at the forefront.^{1,2} The last two decades' effort, triggered by commercialization of the LiCoO₂-graphite battery by SONY® in 1991, has led to the exploration and commercialization of various transition metal oxide cathodes (e.g. LiMn₂O₄, LiMn_{3/2}Ni_{1/2}O₄, LiCo_{1/3}Mn_{1/3}Ni_{1/3}O₂) along with a myriad of polyanionic compounds.^{3,4} With the advent of olivine LiFePO₄ in 1997,⁵ electrochemists have tried and tested families of polyanionic cathodes such as borates (LiMBO₃), silicates (Li₂MSiO₄), fluorophosphates (LiMPO₄F) and fluorosulphate (LiMSO₄F) *etc.*⁶⁻¹⁰ Although many such systems have formidable electrochemical performance, they suffer from low kinetics, inconvenient synthesis, atmospheric poisoning and/or low redox voltage. From applications point of view, the PO₄-based systems are the most suitable cathodes owing to their robust structure, ease of synthesis, economy and good thermal/chemical stability.

Besides olivine LiMPO₄, the alkali metal pyrophosphates ($A_2MP_2O_7$; $A = \text{Li/Na}$, $M = \text{transition metals}$) form a diphosphate (P₂O₇ *i.e.* PO₄-PO₄) family of compounds showing rich structural diversity and the widest range of redox potential (2.0~4.9 V).¹¹ Over the last 15 years, numerous lithium-based pyrophosphate compounds, Li_{2-x}MP₂O₇ ($x = 0-1$; $M = \text{Fe/Co/Mn/Ni/V/Ti}$), have been reported as potential cathode materials.¹²⁻¹⁶ In contrast, there has been no report on electrochemical activity of any sodium-based pyrophosphate (Na₂MP₂O₇) cathode compound, though they have been investigated by crystallographers for over four decades.¹¹ With the current renewed interest in sodium-ion batteries for economic large-scale energy storage systems, inorganic chemists have tried to unravel new Na-based oxide and polyanionic insertion compounds.¹⁷ Putting the pyrophosphate framework compounds on anvil, we have recently discovered two novel (3.0 V) electrochemically active sodium-based cathodes: Na₂CoP₂O₇ and Na₂FeP₂O₇.^{18,19}

Though these pyrophosphate oxyanionic compounds have been intensely studied focusing on their ionic and electrochemical properties, there is also a dearth of detailed analyses of their magnetic properties. Fundamental investigation of magnetic structure of cathode compounds can reveal interesting physical phenomena like magneto-electric effect, geometric frustration, non-collinearity and magneto-dielectric coupling.²⁰ As a

first step in our effort to investigate a series of PO₄-based cathode materials, here we report the magnetic structure and physical properties of Na₂CoP₂O₇ cathode compound. Na₂CoP₂O₇ forms an interesting system showing structural complexity and distinct polymorphism, namely 3D-framework (*pink* form) and layered (*blue* form) systems.²¹⁻²³ We have probed the magnetic structural analysis of the layered-Na₂CoP₂O₇ with close ensemble of CoO₄ tetrahedra. Using temperature-dependent magnetic susceptibility, we have observed a very low magnetic transition temperature (6.5 K). Further, employing neutron powder diffraction study, we propose a G-type non-collinear antiferromagnetic Co-spin configuration.

Experimental Section:

Material Synthesis: The Na₂CoP₂O₇ powder sample was synthesized by conventional solid-state synthesis using a stoichiometric 2:1 molar mixture of NaH₂PO₄ (Wako, 99%) and CoC₂O₄ (Kojundo, 99+%). These precursors were intimately mixed by wet planetary ball-milling in acetone media for 1 h (600 rpm) employing Cr-hardened stainless steel (Cr-SS) milling media and container. After drying out the acetone, the precursor mixture was ground in an agate mortar, pelletized and sintered at 600 °C (heating rate = 10 °C/min) for 6 h in a tubular furnace under steady argon flow to obtain the desired phase.

Structural Analysis: High precision powder X-ray diffraction (XRD) analysis was performed on polycrystalline Na₂CoP₂O₇ using a Bruker AXS D8 ADVANCE diffractometer (operating at 35 mA, 40 kV) equipped with a Co-K α source ($\lambda_1 = 1.78897$ Å, $\lambda_2 = 1.7929$ Å) and a Vantec-1 linear position sensitive detector. The scan was performed in the 2θ range of 10~70° (at 0.5°.min⁻¹). The XRD data analysis confirmed complete formation of desired phase with no impurity and an orthorhombic (space group #33, *Pna2*₁) structure.

Magnetic Susceptibility and Specific Heat Measurement: Magnetic susceptibility and heat capacity measurements of Na₂CoP₂O₇ were conducted employing a Quantum Design PPMS instrument. The susceptibility was recorded in field-cooled (FC) and zero field cooled (ZFC) modes in an applied field of 50 kOe over the temperature range 2–300 K. Magnetization data as a function of field were collected to ± 100 kOe at 2 K. Heat

capacity measurements were performed on a $\text{Na}_2\text{CoP}_2\text{O}_7$ pellet over the temperature range 2–50 K.

Neutron Powder Diffraction: Neutron powder diffraction (NPD) data were collected on the high-resolution powder diffractometer Echidna at the OPAL facility (Lucas Height, Australia) using neutrons of wavelength 2.4395 Å. The high intensity of Echidna offers excellent resolution at low angle, enabling the magnetic structure determination. For the measurements, a ~2 g powder sample was loaded into a 6 mm diameter cylindrical vanadium can, and data collected between 300 K and 3 K using a closed-cycle refrigerator. Rietveld analysis²⁴ for magnetic structure determination was conducted using the FullProf²⁵ suite with the default neutron scattering lengths and Co^{2+} magnetic form-factors.

Results and Discussion:

Crystal Structure: $\text{Na}_2\text{CoP}_2\text{O}_7$ has been reported to exist in three distinct polymorphs: triclinic ($P1$), orthorhombic ($Pna2_1$) and tetragonal ($P4_2/mnm$) phases.²¹⁻²³ While the triclinic phase is thermodynamically most unstable, both tetragonal and orthorhombic polymorphs, having similar structure, have been proposed as the most thermodynamically stable phase. However, our extensive synthetic investigation produced only the orthorhombic polymorph in every case independent of sintering temperature (500-800 °C), heating rate (1-10 °/min) and annealing time (1~24 h). This polymorph is a layered structure with layers of mixed Co and P tetrahedral (i.e. CoO_4 and PO_4) units forming $[\text{Co}(\text{P}_2\text{O}_7)]^{2-}$ slabs parallel to (001), which are stacked with alternating layers of sodium atoms (**Figure 1**). The Co species are linked to four oxygen atoms in tetrahedral fashion, one each from four surrounding PO_4 units with the average Co–O bond length of 1.98(2) Å. When viewed along the (010) direction, the distinct organization of Na and Co channels is evident with each Co channel being surrounded by four sodium channels. This layered compound presents continuous channels for Na-cation movement, responsible for the efficient Na (de)intercalation properties discovered recently.¹⁹

It should be noted that the orthorhombic $Pna2_1$ modification of $\text{Na}_2\text{CoP}_2\text{O}_7$ is only a slightly distorted version of the tetragonal $P4_2/mnm$ form and can be related to the latter *via* the cell axes transformation ($2b,c,a$) and origin shift by ($x\sim 0,3/4,1/4$). This fact

has implications for the magnetic structure analysis as discussed below and also suggests that there may be a crystal structural displacive phase transition between the orthorhombic and tetragonal modifications at elevated temperature, which will be investigated in the near future. In addition, previous reports of the tetragonal form of $\text{Na}_2\text{CoP}_2\text{O}_7$ at room temperature²¹⁻²³ hint that the tetragonal form can probably be quenched or stabilized by deviations from the ideal stoichiometry.

The orthorhombic distortion of the unit cell defined as $(a_{\text{orth}}/2 - c_{\text{orth}})/(a_{\text{orth}}/2 + c_{\text{orth}})$ is rather small, $7.1 \cdot 10^{-6}$ and $5.9 \cdot 10^{-5}$ at 300 K and 3 K, respectively. However, the analysis of the atomic coordinates in the orthorhombic structure with respect to the positions in the undistorted, i.e. tetragonal, form indicates that the atomic displacements within the unit cell are very substantial. Such a quantitative analysis has been done in terms of amplitudes of symmetry-adapted distortion modes using the ISODISTORT software [B. J. Campbell, H. T. Stokes, D. E. Tanner, D. M. Hatch, J. Appl. Cryst. 39, 607--614 (2006)]. The amplitude of the X1 distortion mode was found to be by far the largest, i.e. 2.8 Å compared to those for three remaining modes (0.29 Å, 0.71 Å, and 0.71 Å for GM1+, GM2+, and GM5-, respectively) at 300 K. The main effect the X1 mode produces on the crystal structure is anti-phase rotation of $[\text{PO}_4]$ tetrahedra in the adjacent $[\text{CoP}_2\text{O}_7]$ layers, reminiscent of anti-phase octahedra tilting in perovskites. Unsurprisingly, oxygen atoms experience the largest displacements from the ideal positions. The average displacements of Co, P, Na, and O atoms produced by the combination of all 4 distortion modes are 0.14 Å, 0.22 Å, 0.28 Å, and 0.33 Å, with O2, O3, O8, and O12 atoms displacing by as much as 0.47 Å, 0.46 Å, 0.54 Å, and 0.43 Å, respectively.

The final Rietveld fit to 300 K NPD data is presented in **Figure 2** and the resulting crystallographic information is listed in **Table 1**.

Magnetic Susceptibility and Specific Heat of $\text{Na}_2\text{CoP}_2\text{O}_7$:

The FC magnetic susceptibility χ and the corresponding χ^{-1} as a function of temperature for $\text{Na}_2\text{CoP}_2\text{O}_7$ are shown in **Figure 3**. No divergence between FC and ZFC data was observed. The χ plot reveals that the material undergoes a magnetic ordering transition at ~ 6.5 K (Figure 3, inset). The susceptibility above 50 K follows the Curie-Weiss law with $\theta_{\square} = -16.1$ K and $C = 2.56$. The negative θ indicates predominantly

antiferromagnetic (AFM) interactions between cobalt atoms. The plot of magnetization vs. field plot at 2 K (**Figure 4**) is a perfect straight line with no hysteresis, as expected for a pure antiferromagnet; no evidence for a weak ferromagnetic component or canting of the AFM moments at low temperatures is observed. The effective magnetic moment μ_{eff} calculated from the Curie constant is $4.55 \mu_{\text{B}}$, which exceeds the spin-only value of $3.87 \mu_{\text{B}}$ expected for a Co^{2+} (d^7) ion in high-spin (or any other) configuration. This is a typical for divalent cobalt atoms, due to partially unquenched spin-orbit coupling which allows a contribution from orbital angular momentum.

It may be interesting to compare the magnetic behavior of different polymorphs of $\text{Na}_2\text{CoP}_2\text{O}_7$. Although no magnetic data were reported for the triclinic “pink form”²¹, the deviation of the magnetic susceptibility from the Curie-Weiss behavior previously observed for the “blue form” below 10 K was attributed to the onset of antiferromagnetic interactions in the Co^{2+} sublattice²². Unfortunately, since the magnetic measurement was not complemented by a low-temperature crystal structural study, it is impossible to tell whether the sample was tetragonal or orthorhombic in the vicinity of 10K. We note however, that in the subsequent electronic paramagnetic resonance (EPR) study of the “blue form” by the same authors²³ tetragonal symmetry was found insufficient to explain the EPR data at low temperature and orthorhombic symmetry of Co^{2+} sites was proposed as the origin of the observed complex spectrum²³. This supports our results indicating that at low temperature a stable form of $\text{Na}_2\text{CoP}_2\text{O}_7$ is orthorhombic which undergoes a magnetic transition around 6.5 K.

The specific heat data for $\text{Na}_2\text{CoP}_2\text{O}_7$ (**Figure 5**) shows a λ -type anomaly at ~ 6.5 K indicative of a long-range magnetic ordering transition, in agreement with the magnetic susceptibility data. The magnetic contribution to heat capacity was obtained by subtracting the phonon contribution from the experimental data. Since no heat capacity data are available for a non-magnetic analogue of $\text{Na}_2\text{CoP}_2\text{O}_7$, we estimated the lattice contribution using the Debye model:

$$c_{\text{phon}}(T, \theta_D) = 9R \left(\frac{T}{\theta_D} \right)^3 \int_0^{\theta_D/T} \frac{x^4 e^x}{(e^x - 1)^2} dx,$$

where R is the gas constant and θ_D is the Debye temperature.

Furthermore, to account for the significant difference in atomic masses of the elements constituting $\text{Na}_2\text{CoP}_2\text{O}_7$, the experimental data were analyzed using a model

with two phonon spectra $c_{phon} = 3c_{phon,1}(T, \theta_{D,1}) + 9c_{phon,2}(T, \theta_{D,2})$ with the first and second terms corresponding to Co/P and Na/O contributions, respectively. The fit (Figure 5) to the high-temperature range of the experimental data ($T > 40$ K) yielded $\theta_{D,1}$ and $\theta_{D,2}$ equal to 654 K and 196 K, respectively, which is consistent with the lighter element sublattice having the higher Debye temperature. As can be also seen in Figure 5, non-zero $C_{p,mag}$ signal appears at temperatures significantly above the λ -type anomaly. The overall shape of the magnetic heat capacity curve in combination with the negative θ_{CW} suggest that $\text{Na}_2\text{CoP}_2\text{O}_7$ is a 3D antiferromagnetic Heisenberg system with weakly coupled planes.²⁶ Although the variation in Co-Co distances due to low symmetry of the crystal structure made it impossible to extract values of magnetic exchange parameters, this was further corroborated by the results of the neutron diffraction data analysis.

Finally, the magnetic entropy was calculated as $S_{mag} = \int_0^T C_{p,mag}/T dT$ with $C_{p,mag}$ extrapolated between the lowest measured temperature (2 K) and 0 K as $C_{p,mag} \propto T^3$ assuming a spin-wave model for a 3D antiferromagnet.²⁷ The total magnetic entropy saturates at the value $10 \text{ J}\cdot\text{mol}^{-1}\cdot\text{K}^{-1}$, consistent with the theoretical value $S_{mag} = R\ln(2S+1) = 11.5 \text{ J}\cdot\text{mol}^{-1}\cdot\text{K}^{-1}$ for Co^{2+} in the 3/2 spin state. It is worth noting that only approximately one-third of the total entropy is gained at T_N , which also suggests that the λ -type anomaly at 6.5 K is associated with 3D ordering, while at higher temperature the magnetic entropy is associated with short-range 2D correlations.

Magnetic Structure from Neutron Powder Diffraction Measurements:

The magnetic susceptibility and heat capacity data suggest a long-range magnetic transition around 6.5 K. Indeed, examination of the neutron diffraction data collected at 3, 5, 7, 9, 11, 13, and 300 K reveal additional intensity, presumably due to antiferromagnetic ordering, developing below 7 K (**Figure 6**). All diffraction peaks with magnetic scattering contributions could be indexed to the crystallographic unit cell, *i.e.*, with the propagation vector $k = (0,0,0)$. For the two cobalt $4a(x,y,z)$ Wyckoff sites of the $Pna2_1$ space group, the magnetic representation decomposes in terms of four one-dimensional irreducible representations (IR) as $\Gamma = 3\Gamma_1 + 3\Gamma_2 + 3\Gamma_3 + 3\Gamma_7$. The associated basis vectors are listed in **Table 2**.

Preliminary analysis indicated that the $\Gamma 1$ and $\Gamma 3$ IRs provide the best agreement with the experimental NPD data with A_x and A_z being the primary ordering modes, respectively. Careful examination of the data also revealed much weaker magnetic peaks corresponding to C_z and C_x modes, respectively (Figure 6), while no evidence of the modes defining the moment component along y -axis was found.

The fact that the $\Gamma 1$ ($A_x, 0, C_z$) and $\Gamma 3$ ($C_x, 0, A_z$) models produced similar agreement is not surprising given the pseudo-tetragonal nature of the crystal structure. In the ideal tetragonal form, NPD data analysis would not have been able to distinguish the direction of the moment in the $a_{\text{tetr}}b_{\text{tetr}}$ -plane. However, for the $Pna2_1$ orthorhombic modification, the displacements of cobalt atoms from their ideal positions are apparently sufficient for the NPD data analysis to favor the $\Gamma 3$ ($C_x, 0, A_z$) model based on the R_{mag} -factor (6.69% vs. 7.68% for the $\Gamma 1$ ($A_x, 0, C_z$) model). Therefore, we used the $\Gamma 3$ ($C_x, 0, A_z$) model, equivalent to the $Pn'a2_1'$ Shubnikov group, in the further discussion.

For refinements against the NPD data collected at 3 K, this model yielded components of the magnetic moment along a_{orth} , b_{orth} , and c_{orth} axes 1.09(7), 0 and 2.71(3) μ_B , respectively, which translates to a total moment of 2.92(4) μ_B , very close to the spin-only value of 3 μ_B expected for the $3d^7$ configuration of Co^{2+} , and the canting angle from the c -axis in the ac -plane of 22(1) $^\circ$. The final Rietveld plot and the magnetic structure are shown in **Figures 7 and 8**, respectively, with corresponding structural parameters listed in **Table 3**.

The magnetic structure can be well rationalized by considering the mutual arrangement of the metal sites and exchange paths. Despite the low symmetry and layered nature of the crystal structure, the Co^{2+} atoms are located on a pseudo-cubic lattice with Co-Co distances in the range 5.1-5.6 Å (**Figure 8b**). In fact, the inter-layer Co-Co distances are slightly shorter than the those within the $[\text{CoP}_2\text{O}_7]_\infty$ slabs.

Although the cobalt-oxygen tetrahedra share neither edges nor corners, they are linked *via* the phosphate groups in the ac -plane that open Co-O-O-Co super-superexchange paths with the large Co-O-O angles, favoring antiferromagnetic interactions (Figure 8c). As a result, the material orders into a slightly non-collinear variation of antiferromagnetic G-type, as can be seen in Figure 8b highlighting the nearest neighbors of one of the cobalt atoms. We find it especially significant that despite similar inter- and intralayer Co-Co distances, the shortest O-O distance between layers is

substantially longer than the O-O distances within the $[\text{CoP}_2\text{O}_7]_\infty$ slabs (~ 2.9 Å vs. ~ 2.5 Å, respectively). In fact, the former value is just above the van der Waals distance of 2.8 Å, which is considered to be a threshold for successful super-superexchange *via* O-O contacts.²⁸ The implications of this difference in O-O intra- and interlayer distances is consistent with the heat capacity data discussed above; *i.e.*, below ~ 40 K, stronger super-superexchange within $[\text{CoP}_2\text{O}_7]_\infty$ layers results in short-range 2D magnetic correlations and cooling to much the lower temperature of 6.5 K is required to extend the interactions in the third dimension and establish a long-range 3D antiferromagnetic structure.

Conclusions:

In this article, we have reported the magnetic structure of $\text{Na}_2\text{CoP}_2\text{O}_7$ sodium-ion cathode compound. The magnetic susceptibility follows a Curie-Weiss behavior above 50 K with $\theta = -16.1$ K. Magnetic measurements reveal an antiferromagnetic ordering in $\text{Na}_2\text{CoP}_2\text{O}_7$ at $T_N = 6.5$ K. Neutron powder diffraction pattern at 3 K shows that the Co spins in each $[\text{CoP}_2\text{O}_7]_\infty$ layers are antiferromagnetically coupled and the Co spins in adjacent $[\text{CoP}_2\text{O}_7]_\infty$ layers are arranged in a non-collinear manner.

Acknowledgements:

The current work is partially supported by the ‘Element Strategy Initiative for Catalysts & Batteries’ (ESICB) project by the Ministry of Education, Culture, Sports, Science and Technology, Japan (MEXT). PB acknowledges the Japan Society for the Promotion of Sciences for a JSPS Fellowship at the University of Tokyo. CDL’s contribution was supported by the Australian Research Council (DP110102662). The crystal structure has been drawn using the VESTA software.²⁹

References:

1. Goodenough, J.B.; Kim, Y. *Chem. Mater.* **2010**, *22*, 587-603.
2. Etacheri, V.; Marom, R.; Elazari, R.; Salitra, G.; Aurbach, D. *Energy Environ. Sci.* **2011**, *4*, 3243-3262.
3. Desilvestro, J.; Haas, O. *J. Electrochem. Soc.* **1990**, *137*, 5-22.
4. Gong, Z.; Yang, Y. *Energy Environ. Sci.* **2011**, *4*, 3223-3242.
5. Padhi, A.K.; Nanjundaswamy, K.S.; Goodenough, J.B. *J. Electrochem. Soc.* **1997**, *144*, 1188-1194.
6. Yamada, A.; Iwane, N.; Harada, Y.; Nishimura, S.; Koyama, Y.; Tanaka, I. *Adv. Mater.* **2010**, *22*, 3583-3587.
7. Nyten, A.; Abouimrane, A.; Armand, M.; Gustafsson, T.; Thomas, J.O. *Electrochem. Commun.* **2005**, *7*, 156-160.
8. Ramesh, T.N.; Lee K.T.; Ellis, B.E.; Nazar, L.F. *Electrochem. Solid-State Lett.* **2010**, *13*, 43-47.
9. Recham, N.; Chotard, J.N., Dupont, L.; Delacourt, C.; Walker, W.; Armand, M.; Tarascon, J.M. *Nature Mater.* **2010**, *9*, 68-74.
10. Barpanda, P.; Ati, M.; Melot, B.C.; Rouse, G.; Chotard, J.N.; Doublet, M.L.; Sougrati, M.T.; Corr, S.A.; Jumas, J.C.; Tarascon, J.M. *Nature Mater.* **2011**, *10*, 772-779.
11. Barpanda, P.; Nishimura, S.; Yamada, A. *Adv. Energy Mater.* **2012**, *2*, 841-859.
12. Padhi, A.K.; Nanjundaswamy, K.S.; Masquelier, C.; Okada, S.; Goodenough, J.B. *J. Electrochem. Soc.* **1997**, *144*, 1609-1613.
13. Nishimura, S.I.; Nakamura, M.; Natsui, R.; Yamada, A. *J. Am. Chem. Soc.* **2010**, *132*, 13596-13597.
14. Tamaru, M.; Barpanda, P.; Yamada, Y.; Nishimura, S.I.; Yamada, A. *J. Mater. Chem.* **2012**, *22*, 24526-24529.
15. Kim, H.; Lee, S.; Park, Y.U.; Kim, H.; Kim, J.; Jeon, S.; Kang, K. *Chem. Mater.* **2011**, *23*, 3930-3937.
16. Uebou, Y.; Okada, S.; Egashira, M.; Yamaki, J. *Solid State Ion.* **2002**, *148*, 323-328.
17. Palomares, V.; Serras, P.; Villaluenga, I.; Hueso, K.B.; Gonzalez, J.C., Rojo, T. *Energy Environ. Sci.* **2012**, *5*, 5884-5901.

18. Barpanda, P.; Ye, T.; Nishimura, S.I.; Chung, S.C.; Yamada, Y.; Okubo, M.; Zhou, H.; Yamada, A. *Electrochem. Commun.* **2012**, *24*, 116-119.
19. Barpanda, P.; Yamada, A. Japanese Patent, *JP 2011-193073*.
20. Hagemann, I.S.; Khalifah, P.G.; Ramirez, A.P.; Cava, R.J. *Phys. Rev. B.* **2000**, *62*, R771-R774.
21. Erragh, F.; Boukhari, A.; Elouadi, B.; Holt, E.M. *J. Crystallogr. Spectrosc. Res.* **1991**, *21*, 321-326.
22. Sanz, F.; Parada, C.; Rojo, J.M.; Ruiz-Valero, C.; Saez-Puche, R. *J. Solid State Chem.* **1999**, *145*, 604-611.
23. Beaury, L.; Derouet, J.; Binet, L.; Sanz, F.; Ruiz-Valero, C. *J. Solid State Chem.* **2004**, *177*, 1437-1443.
24. Rietveld, H.M. *J. Appl. Crystallogr.* **1969**, *2*, 65-71.
25. Rodriguez-Carvajal, J. *Physica B* **1993**, *192*, 55-69.
26. Sengupta, P.; Sandvik, A.W.; Singh, R.R.P. *Phys. Rev. B.* **2003**, *68*, 094423.
27. Joshua, S.J. *Physica A* **1998**, *261*, 135-142.
28. Whangbo, M.W.; Koo, H.J.; Dai, D. *J. Solid State Chem.* **2003**, *176*, 417-481.
29. Momma, K.; Izumi, F. *J. Appl. Crystallogr.* **2011**, *13*, 1272-1276.

Table 1. Crystal structural parameter for Na₂CoP₂O₇ at 300 K refined against NPD data. Space group *Pna*2₁ (No 33) with all the atoms in 4a(x,y,z) Wyckoff sites. Numbers in parentheses are standard deviations of the last significant digit. $a = 15.4061(3)$ Å, $b = 10.28854(9)$ Å, $c = 7.70316(15)$ Å, $V = 1221.00(3)$ Å³, overall isotropic temperature factor $B = 0.76(5)$ Å².

| Atom | x | y | z |
|------|-------------|------------|-------------|
| Co1 | 0.129(3) | 0.507(4) | -0.529(6) |
| Co2 | 0.1231(17) | 0.012(3) | -0.552(6) |
| P1 | 0.1914(5) | 0.0679(7) | -0.9048(10) |
| P2 | 0.0607(5) | 0.0499(7) | -0.1914(10) |
| P3 | 0.0537(5) | 0.4658(7) | -0.1518(10) |
| P4 | 0.1947(5) | 0.4813(6) | -0.9039(11) |
| Na1 | 0.301(2) | 0.2624(19) | -0.706(3) |
| Na2 | -0.0623(20) | 0.2381(18) | -0.406(4) |
| Na3 | 0.2315(17) | 0.2852(17) | -0.231(4) |
| Na4 | 0.0122(13) | 0.239(2) | -0.874(3) |
| O1 | 0.1379(6) | 0.1023(10) | -0.0739(13) |
| O2 | 0.1374(9) | 0.1211(12) | -0.7541(16) |
| O3 | 0.2848(5) | 0.1099(13) | 0.094(2) |
| O4 | 0.1872(10) | -0.0771(7) | -0.888(2) |
| O5 | 0.0698(10) | -0.0952(7) | -0.183(2) |
| O6 | 0.0803(10) | 0.1205(15) | -0.3630(14) |
| O7 | -0.0163(6) | 0.1077(15) | -0.093(2) |
| O8 | 0.1070(6) | 0.4283(12) | -0.9875(12) |
| O9 | -0.0341(6) | 0.3989(15) | -0.139(2) |
| O10 | 0.0456(10) | 0.6092(8) | -0.159(2) |
| O11 | 0.0923(9) | 0.4044(18) | -0.3119(16) |
| O12 | 0.1880(11) | 0.4185(13) | -0.7271(13) |
| O13 | 0.2728(7) | 0.4212(13) | -0.9925(20) |
| O14 | 0.1947(10) | 0.6275(7) | -0.907(3) |

Table 2. Representational analysis for the 4a(x,y,z) Co1 and Co2 sites of the $Pna2_1$ space group and the propagation vector $k=[0,0,0]$. The atomic positions are (x,y,z); (-x,-y,z+1/2); (x+1/2,-y+1/2,z), (-x+1/2,y+1/2,z+1/2). The ordering modes are defined as F(+++), C(++--), G(+--+), A(+--+).

| IR | Basis vectors | Shubnikov group |
|------------|---------------|-----------------|
| Γ_1 | Ax Gy Cz | $Pna2_1$ |
| Γ_2 | Gx Ay Fz | $Pn'a'2_1$ |
| Γ_3 | Cx Fy Az | $Pn'a2_1'$ |
| Γ_4 | Fx Cy Gz | $Pna'2_1'$ |

Table 3. Crystal structural parameter for Na₂CoP₂O₇ at 3 K refined against NPD data. Space group *Pna*2₁ (No 33) with all the atoms in 4a(x,y,z) Wyckoff sites. Numbers in parentheses are standard deviations of the last significant digit. $a = 15.3758(2)$ Å, $b = 10.23927(8)$ Å, $c = 7.68699(11)$ Å, $V = 1210.22(3)$ Å³, overall isotropic temperature factor $B = 0.01(4)$ Å².

| Atom | x | y | z |
|------|-------------|------------|-------------|
| Co1 | 0.132(2) | 0.507(4) | -0.524(5) |
| Co2 | 0.1262(13) | 0.014(3) | -0.565(4) |
| P1 | 0.1902(5) | 0.0709(6) | -0.9080(10) |
| P2 | 0.0611(5) | 0.0526(7) | -0.1962(9) |
| P3 | 0.0542(5) | 0.4646(7) | -0.1488(10) |
| P4 | 0.1956(5) | 0.4798(6) | -0.9037(10) |
| Na1 | 0.301(2) | 0.2714(18) | -0.703(3) |
| Na2 | -0.0616(18) | 0.2335(17) | -0.402(4) |
| Na3 | 0.2305(16) | 0.2821(16) | -0.237(3) |
| Na4 | 0.0108(12) | 0.2408(20) | -0.876(3) |
| O1 | 0.1393(6) | 0.1037(9) | -0.0809(12) |
| O2 | 0.1350(8) | 0.1228(11) | -0.7576(14) |
| O3 | 0.2826(5) | 0.1121(12) | 0.100(2) |
| O4 | 0.1837(9) | -0.0768(7) | -0.8905(18) |
| O5 | 0.0731(9) | -0.0928(7) | -0.186(2) |
| O6 | 0.0757(9) | 0.1224(13) | -0.3714(12) |
| O7 | -0.0129(6) | 0.1096(13) | -0.0873(18) |
| O8 | 0.1068(5) | 0.4267(12) | -0.9833(11) |
| O9 | -0.0333(6) | 0.3937(13) | -0.1359(19) |
| O10 | 0.0433(9) | 0.6090(8) | -0.157(2) |
| O11 | 0.0929(8) | 0.4078(16) | -0.3122(14) |
| O12 | 0.1892(10) | 0.4233(12) | -0.7218(12) |
| O13 | 0.2717(7) | 0.4163(12) | -0.9966(18) |
| O14 | 0.1941(9) | 0.6279(7) | -0.908(2) |

List of Figures:

- Figure 1:** Schematic presentation of layer-structured orthorhombic polymorph of $\text{Na}_2\text{CoP}_2\text{O}_7$ viewed along (100), (010) and (001) planes. The CoO_4 tetrahedra (blue), PO_4 tetrahedra (light grey) and sodium atoms (yellow) are illustrated.
- Figure 2:** Rietveld plot for the $\text{Na}_2\text{CoP}_2\text{O}_7$ neutron powder diffraction data at 300 K. The red crosses, black and green solid lines indicate the observed and calculated curves and their difference, respectively. The black tick marks indicate position of the diffraction peaks. $R_p = 4.00\%$, $R_{wp} = 5.06\%$, $R_{\text{Bragg}} = 4.71\%$, $\chi^2 = 2.58$.
- Figure 3:** Magnetic susceptibility χ and the corresponding χ^{-1} (inset) as a function of temperature for $\text{Na}_2\text{CoP}_2\text{O}_7$ measured with the applied field $H = 50$ kOe.
- Figure 4:** Magnetization as a function of field for $\text{Na}_2\text{CoP}_2\text{O}_7$ measured at 2 K.
- Figure 5:** Top: total (open symbols) and magnetic specific heat (filled symbols) obtained by subtracting the lattice contribution (solid line) for $\text{Na}_2\text{CoP}_2\text{O}_7$. Inset: magnetic entropy (solid line) obtained by integrating $C_{p,\text{mag}}/T$ vs T . The horizontal and vertical lines show the theoretical value for spin $S=3/2$ and ordering temperature, respectively.
- Figure 6:** $\text{Na}_2\text{CoP}_2\text{O}_7$ neutron powder diffraction data collected in the vicinity of the magnetic phase transition. The peaks with additional intensity observed below 7 K are indicated with star symbols. The inset shows the enlarged region to illustrate the presence of the weak peaks corresponding to the C_x mode, see the text (the curve for 13 K was offset for clarity).

Figure 7: Rietveld plot for the $\text{Na}_2\text{CoP}_2\text{O}_7$ neutron powder diffraction data at 3 K. The red crosses, black and green solid lines indicate the observed and calculated curves and their difference, respectively. The two rows of black tick marks indicate position of the nuclear (top) and magnetic (bottom) diffraction peaks. The blue curve in the inset shows magnetic contribution. $R_p = 4.29\%$, $R_{wp} = 5.46\%$, $R_{\text{Bragg}} = 4.36\%$, $\chi^2 = 6.01$, $R_{\text{mag}} = 6.69\%$.

Figure 8: (a) General view of the magnetic structure of $\text{Na}_2\text{CoP}_2\text{O}_7$; (b) Co1 and Co2 sublattices with the atoms numbered in the order used for magnetic structure determination; the nearest coordination of one of the cobalt sites highlighted in blue indicates the closeness of the magnetic structure to the antiferromagnetic G-type; (c) super-superexchange paths between Co1 and Co2 sites with the O-O contacts shorter than 3 Å shown with dashed lines.

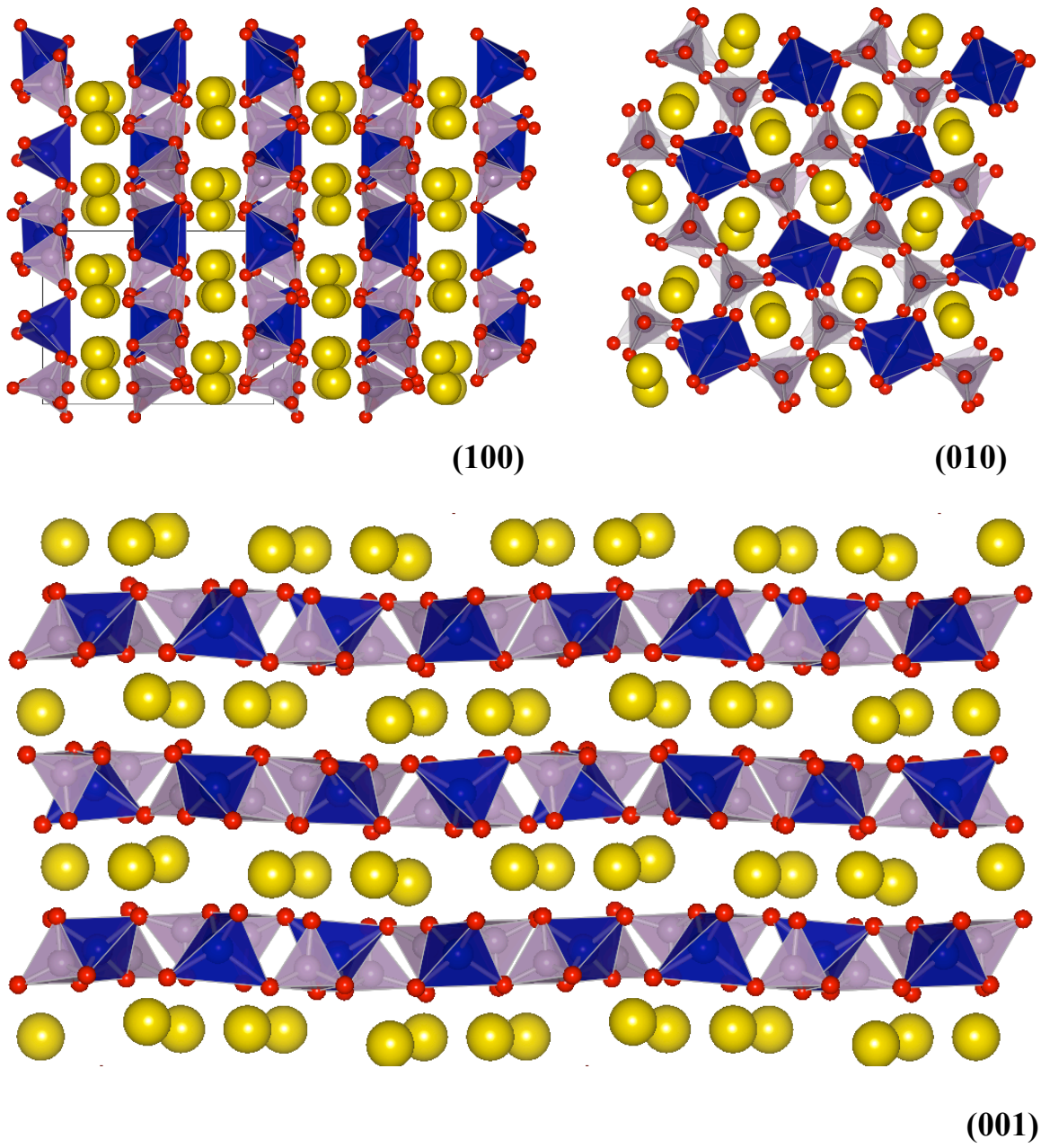


Figure 1.

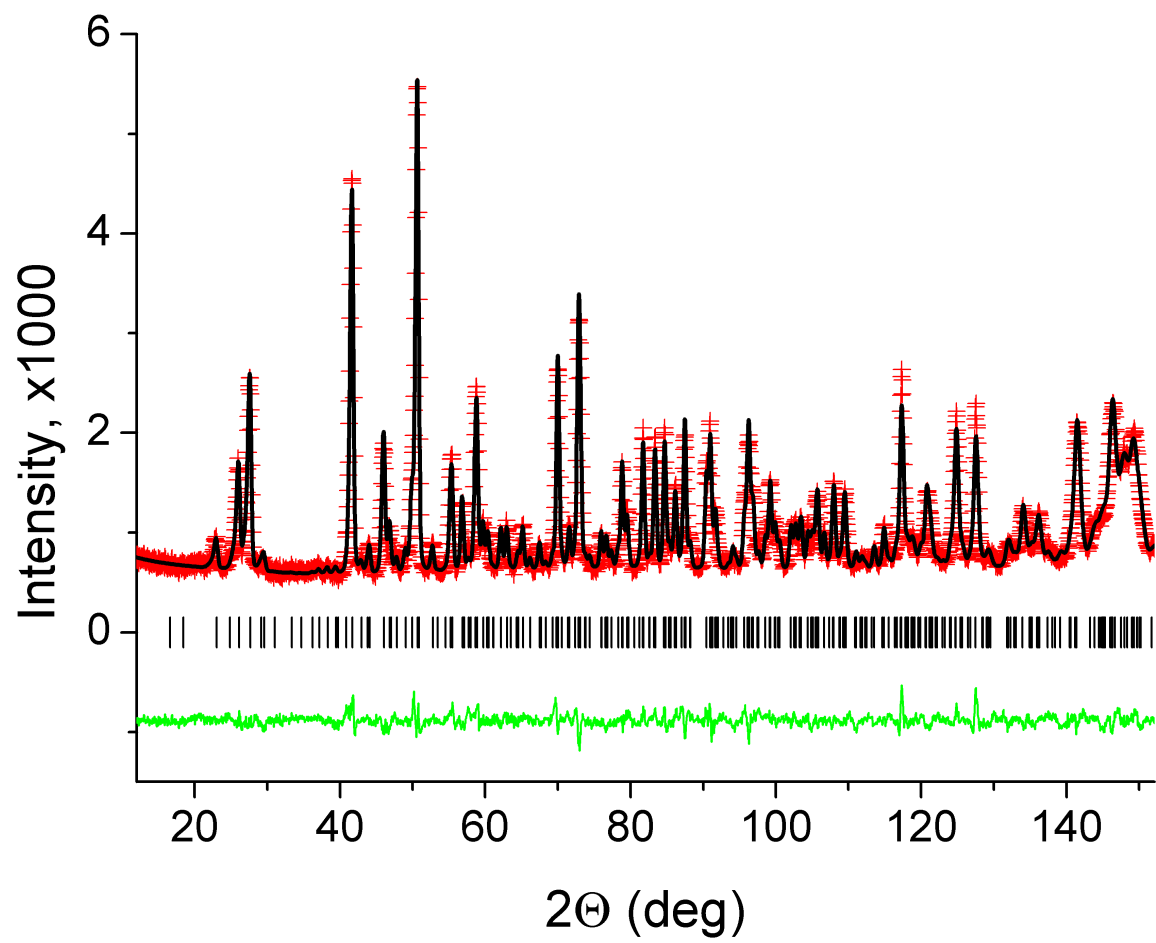


Figure 2.

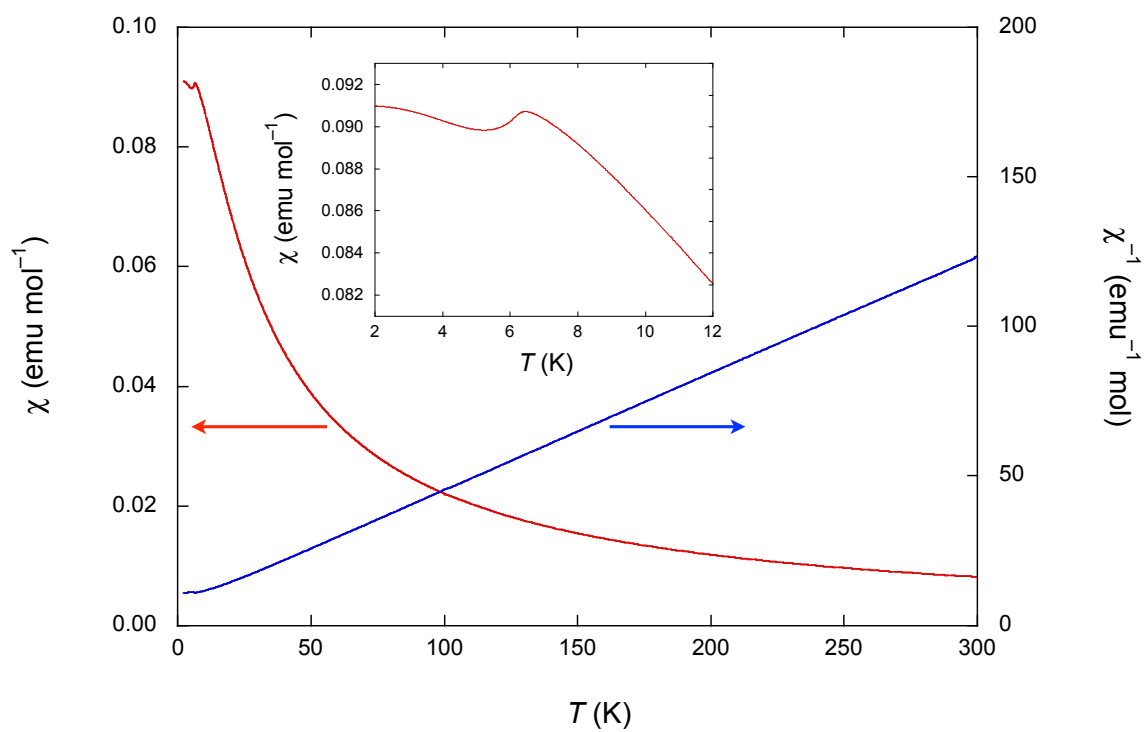


Figure 3.

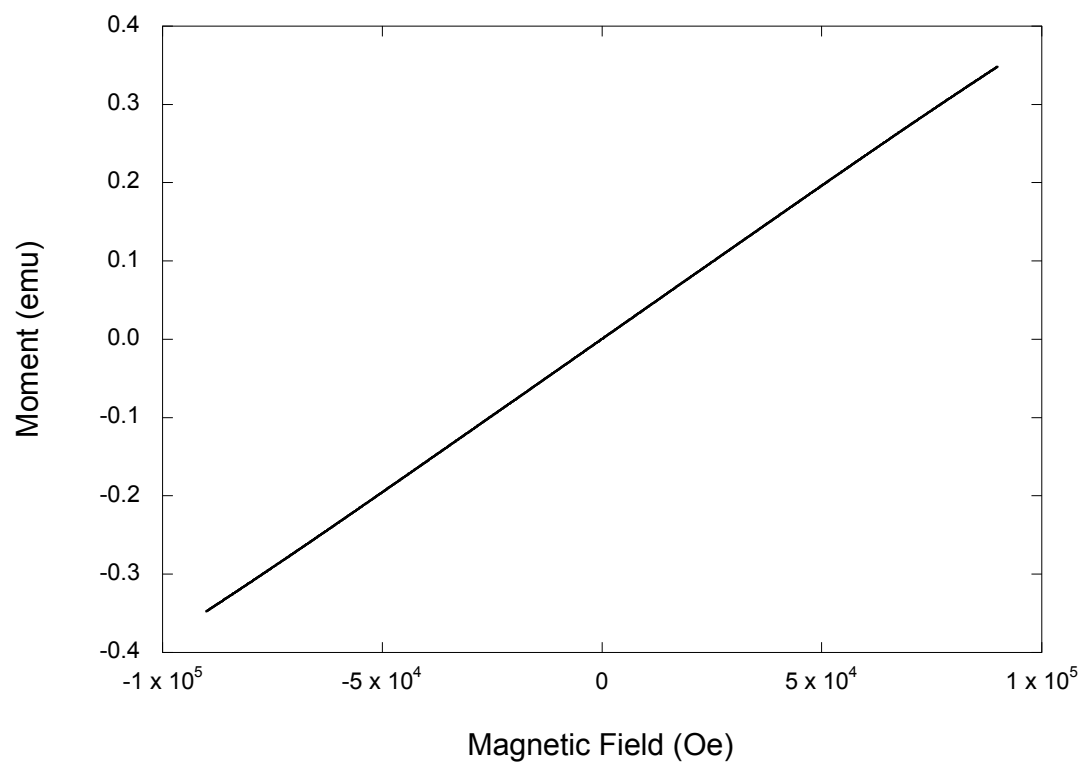


Figure 4.

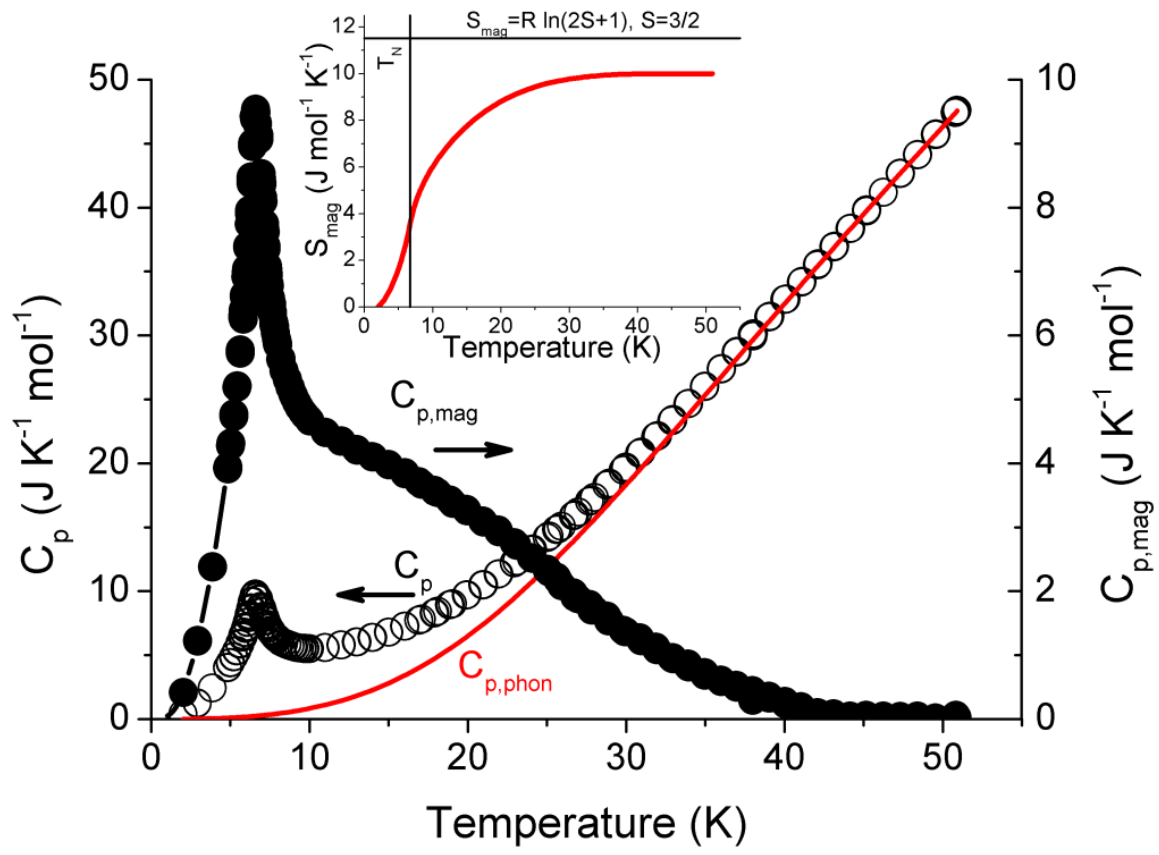


Figure 5.

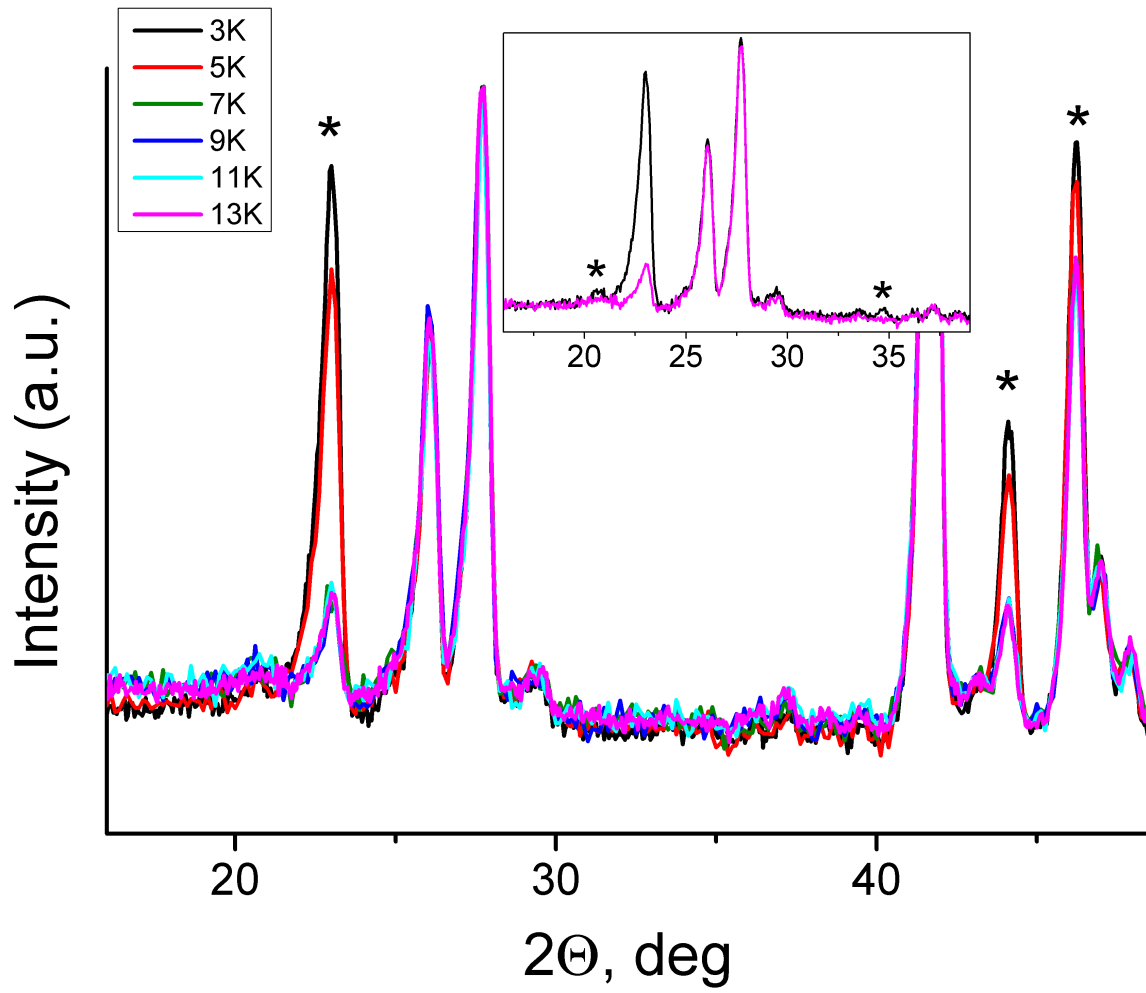


Figure 6.

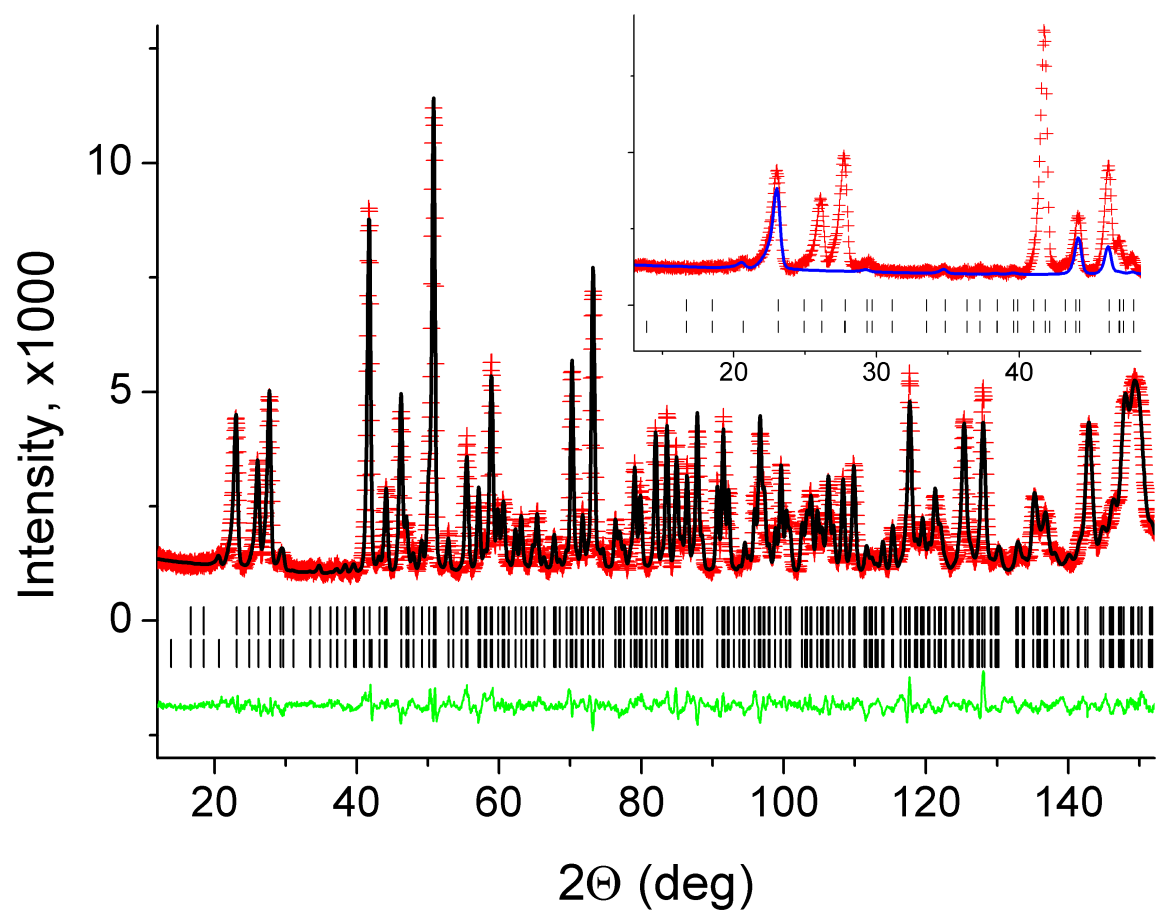


Figure 7.

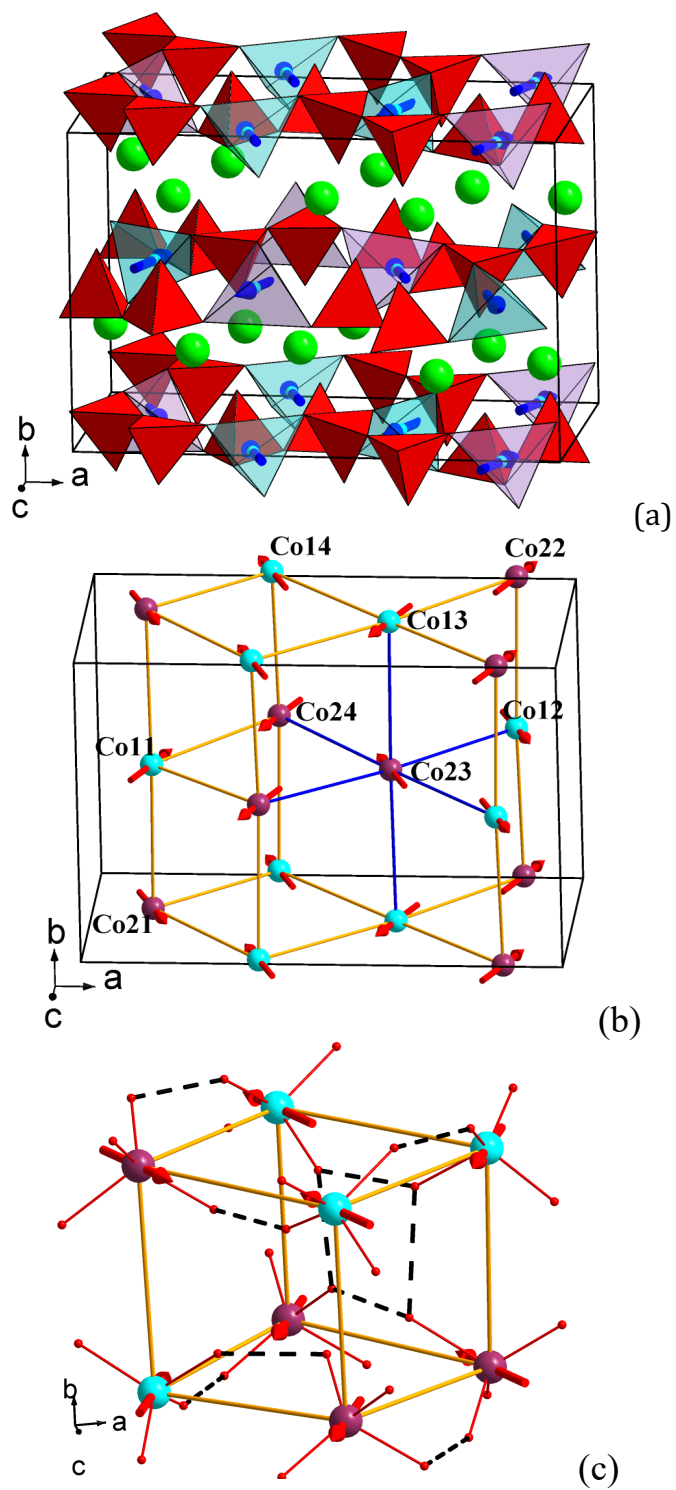


Figure 8.